

PREPARED FOR SUBMISSION TO JINST

25TH INTERNATIONAL WORKSHOP ON RADIATION IMAGING DETECTORS

30 JUNE - 4 JULY 2024

LISBON, PORTUGAL

Test beam results on 3D pixel sensors for the CMS Tracker upgrade at the High-Luminosity LHC

C. Lasaosa^{a,1} on behalf of the CMS Tracker Group

^aIFCA (CSIC-UC), Santander, Spain

E-mail: clara.lasaosa.garcia@cern.ch

ABSTRACT: The High Luminosity upgrade of the CERN Large Hadron Collider (HL-LHC) requires new high-radiation tolerant silicon pixel sensors for the innermost part of the tracking detector in the CMS experiment. The innermost layer of the tracker, which is as close as 3 cm from the interaction point, will be exposed to a fluence of $3.4 \times 10^{16} \text{ n}_{\text{eq}}\text{cm}^{-2}$ during the high-luminosity operation period. The 3D pixel sensor technology has been proven to be the best option for such a layer in terms of radiation tolerance and low power consumption. An extensive program aiming at 3D pixel sensors has been carried out in the context of the CMS tracker R&D activities. The sensors have been produced by Fondazione Bruno Kessler (Trento, Italy) and Centro Nacional de Microelectrónica (Barcelona, Spain). They are connected with the CROCv1 readout chip, which is a prototype of the final version. The modules have been tested in beams at CERN and DESY, before and after irradiation up to an equivalent fluence of about $1.6 \times 10^{16} \text{ n}_{\text{eq}}\text{cm}^{-2}$. An overview of the results obtained in the latest beam test experiments is presented, including hit detection efficiency and spatial resolution. The analysis of collected data shows excellent performance, with around 98% hit detection efficiencies measured after irradiation.

KEYWORDS: HL-LHC, CMS, Tracker, Silicon, 3D pixel sensor, Irradiation, Test beam

¹Corresponding author.

Contents

1	Introduction	1
2	Hybrid 3D pixel silicon modules	2
3	Methodology and test beam results of non-irradiated modules	3
4	Methodology and test beam results of irradiated modules	6
5	Conclusions	7

1 Introduction

The environment of the High-Luminosity Large Hadron Collider (HL-LHC) [1] will feature a peak instantaneous luminosity of $7.5 \times 10^{34} \text{ cm}^{-2}\text{s}^{-1}$ in the ultimate performance scenario, with up to 200 collisions per bunch-crossing on average. This will enable the CMS experiment to collect an integrated luminosity of 4000 fb^{-1} over the project lifetime.

The foreseen radiation levels for the unprecedented high-luminosity scenario lead to the need of upgrading the Compact Muon Solenoid (CMS) experiment. In particular, the innermost region, which is called Inner Tracker (IT) and is made of silicon pixel modules, will be completely replaced. The layer closest to the interaction point will be exposed to a fluence of $3.4 \times 10^{16} \text{ n}_{\text{eq}}\text{cm}^{-2}$, and a total ionising dose of 1.9 Grad will be accumulated during the high-luminosity operation period. A replacement of this layer is planned after approximately six years of operation, at which point it is estimated that a fluence of $1.8 \times 10^{16} \text{ n}_{\text{eq}}\text{cm}^{-2}$ will be reached.

The upgraded CMS IT layout includes an extension of the tracking coverage, optimization of the layer arrangement and reduction of the material budget, among others. It will consist of three substructures as shown in Fig. 1: Tracker Barrel Pixel (TBPX) with four central layers, Tracker Forward Pixel (TFPX) with eight small double discs at each end and Tracker Extended Pixel (TEPX) with four large double discs per side. It will feature hybrid modules with two and four readout chips (ROCs) and it is designed to allow for module replacement if needed.

High radiation tolerance, low power dissipation, increased granularity for improved spatial resolution, and high hit detection efficiency have been crucial requirements in sensor optimization due to the more demanding operational conditions of the HL-LHC. Consequently, the baseline design consists of n-in-p silicon pixel sensors with an active thickness and a pixel cell size reduced to $150 \mu\text{m}$ and $25 \times 100 \mu\text{m}^2$, respectively. For sensor technology, 3D pixels have been selected as the optimal choice for the innermost layer of the TBPX, while planar pixels will be employed elsewhere. This selection is based on detailed simulations that indicate thermal runaway issues with planar sensors in the innermost layer.

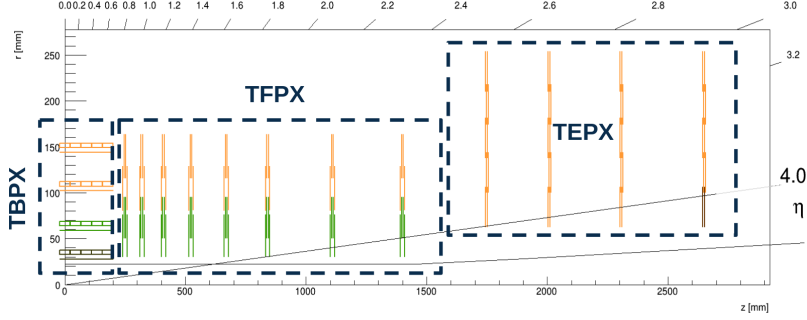


Figure 1: One quarter of the upgraded IT layout in the longitudinal view. Planar pixel modules with two and four ROCs are depicted in orange and green, respectively. 3D pixel modules with two ROCs are represented in black.

2 Hybrid 3D pixel silicon modules

3D pixel sensors [2] consist of cylindrical electrodes that penetrate the bulk perpendicularly as shown in Fig. 2a. This design decouples the thickness from the inter-electrode distance, resulting in a lower depletion voltage which reduces the power consumption. Moreover, the shorter collection path for charge carriers leads to increased charge collection efficiency after irradiation.

There have been two manufacturers involved in the R&D program of the 3D pixel technology for the high-luminosity upgrade of the CMS Tracker: Fondazione Bruno Kessler (FBK) [3] along with Istituto Nazionale di Fisica Nucleare (INFN) in Italy, and Centro Nacional de Microelectrónica (CNM) [4] in Spain. The main differences between the devices of both foundries are the column diameter, which is $5\ \mu\text{m}$ in FBK and $8\ \mu\text{m}$ in CNM, as well as the n^+ -column length, which is approximately $115\ \mu\text{m}$ in FBK and $130\ \mu\text{m}$ in CNM.

In hybrid modules, the sensor is connected to the front-end electronics through the bump-bonding technique. The CMS ROC (CROC) [5], developed by the RD53 Collaboration, is based on 65 nm CMOS technology and features an analog linear front-end whose schematic is shown in Fig. 2b. The readout signal passes through a charge-sensitive amplifier with a Krummenacher feedback loop, which provides a linear discharge of the capacitor. The output signal is then compared against a trimmable threshold for digital conversion using a Time-Over-Threshold (ToT) counter. The matrix is arranged in 432×336 square pixels with $50\ \mu\text{m}$ -pitch. All the single-chip devices, which have been tested and whose results are shown in the following sections, feature the prototype of the final chip called CROCv1. For successful operation, a set of calibrations is performed to tune the modules to a low threshold while keeping the number of masked pixels minimal.

Table 1 includes a list of the modules with details about the irradiation and test beam campaigns. The irradiation of the 3D pixel modules was performed at Karlsruhe Institute of Technology (KIT) with protons at 25 MeV and at the CERN Proton Synchrotron (PS) with protons at 24 GeV. The data taking was carried out at two facilities using different kinds of test beams: at Deutsches Elektronen-Synchrotron (DESY) with an electron/positron beam at 5.2 GeV and at the CERN Super Proton Synchrotron (SPS) with a pion beam at 120 GeV. The test beam setup, similar at both facilities, consists of a EUDET-type telescope [6] with downstream and upstream triplets embedded with Mimosas26 sensors, which feature square pixels with a $18.4\ \mu\text{m}$ -pitch. The system is also equipped

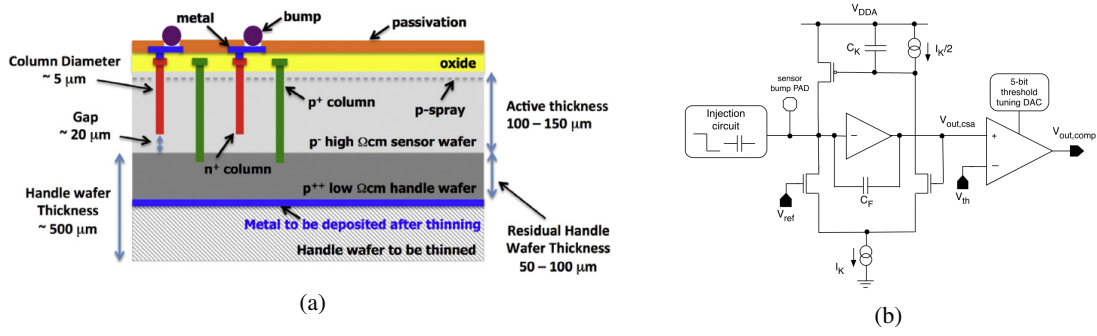


Figure 2: (a) FBK 3D pixel sensor layout, and (b) schematic of the CMS analog linear front-end.

with a Trigger Logic Unit (TLU) that provides the trigger signal and a reference pixel module to filter out out-of-time tracks, which might be reconstructed by the telescope planes due to their long integration time. The Devices Under Test (DUTs) are placed within a cold box located between both telescope arms over a stage that allows rotation and translation of the modules to different positions. The cold box keeps the modules at low temperatures, which is crucial after irradiation.

Table 1: Summary of the single-chip 3D pixel devices that have been tested on beam and whose results are shown in the following sections.

Module name	Sensor manufacturer	Pixel size [μm^2]	Fluence [$\text{n}_{\text{eq}} \cdot \text{cm}^{-2}$]	Irradiation facility	Test beam area	
					non-irradiated	irradiated
CROC_CNM_1	CNM	50×50	-	-	SPS	-
CROC_CNM_2	CNM	25×100	1×10^{16}	PS	SPS	SPS
CROC_FBK_1	FBK	25×100	-	-	SPS	-
CROC_FBK_2	FBK	25×100	1×10^{16}	PS	SPS	SPS
CROC_FBK_3	FBK	25×100	1×10^{16}	PS	SPS	SPS
CROC_FBK_4	FBK	25×100	1.6×10^{16}	KIT	-	DESY

3 Methodology and test beam results of non-irradiated modules

The performance of several non-irradiated modules was investigated using test beam. The main four consist of 3D pixel sensors with $25 \times 100 \mu\text{m}^2$ pixel size, from either FBK or CNM productions. The most salient differences between the two manufacturers mentioned in Section 2 are discussed below. Moreover, results from a CNM sample with $50 \mu\text{m}$ -pitch are included, as this cell design was under consideration during the early stages of the R&D program.

The module thresholds were tuned at a temperature of -10°C to an average pixel threshold of either $1000 e^-$ or $1200 e^-$, depending on the sample. In all devices, the percentage of pixels masked during tuning and before data acquisition was below 1%. Pixels were masked if they were either stuck or noisy. A stuck pixel does not respond to charge injections, while a noisy pixel exhibits a per-pixel occupancy higher than 2×10^{-5} in the absence of injected charge.

The clustering algorithm groups adjacent pixels hit by the passage of a single particle into a cluster, estimating the cluster position as the charge-weighted mean of the individual pixel positions

(see Fig. 3a). The cluster size corresponds to the number of hit pixels, while the cluster charge is determined by the sum of the individual pixel charges. Figure 3b shows the cluster charge distribution of module CROC_FBK_2 above full depletion (30 V) at normal beam incidence. The distribution is fitted to a Landau distribution convoluted with a Gaussian, and the most probable value (MPV) is approximately $11\,000\text{ e}^-$, consistent with the expectation from simulations.

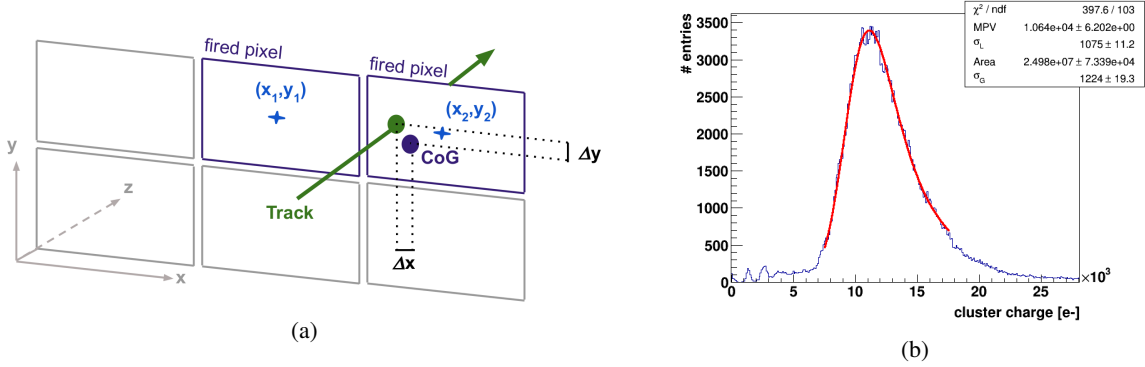


Figure 3: (a) Schematic representation of clustering. The individual hit pixel positions are denoted by (x_i, y_i) . The track and cluster positions are represented by green and violet filled circles. Δx and Δy indicate the residuals along both axes. (b) Cluster charge distribution for module CROC_FBK_2 fitted to a Landau with most probable value MPV and width σ_L , convoluted with a Gaussian of width σ_G .

The hit detection efficiency is defined as the ratio of the number of tracks with an associated hit on the DUT to the total number of tracks. For tracks to be considered, they must have an associated hit on all telescope planes and on the reference module. Additionally, a bunch-crossing restriction and a track isolation criterion are applied to the reference module to ensure high-quality tracks. Figure 4a shows efficiency above 97% at normal beam incidence after full depletion, which happens at a bias voltage of 5 V or even lower in some modules. The higher efficiency of FBK sensors compared to CNM sensors is attributed to the smaller radius of their electrodes, which are made of passive material. Figures 4b and 4c show the efficiency cell maps for module CROC_CNМ_2 at bias voltages below (2 V) and above (30 V) full depletion, respectively. These maps illustrate the progression of depletion from the central n^+ -column towards the corners of the pixel cell, where the ohmic columns are located.

The cluster size is closely related to the spatial resolution of the devices. Figure 5a shows the average cluster size as a function of bias voltage. The cluster size increases as the electric field extends to the periphery of the pixel cell, until the devices are fully depleted. Beyond the full depletion voltage, the electric field becomes strong enough to limit the charge sharing due to diffusion, leading to a decrease in cluster size at the periphery. This effect is clearly illustrated in the cluster size cell maps shown in Figs. 5b and 5c, corresponding to module CROC_FBK_1 at full depletion (5 V) and above full depletion (30 V), respectively. A plausible explanation for the increased cluster size at higher bias voltages is the generation of microavalanches; when the bias voltage significantly exceeds the full depletion voltage, the electric field may become strong enough to artificially enlarge the cluster size. The cluster size of the $50\ \mu\text{m}$ -pitch sensor is notably smaller because the configuration of the electric field in this cell type results in less charge sharing.

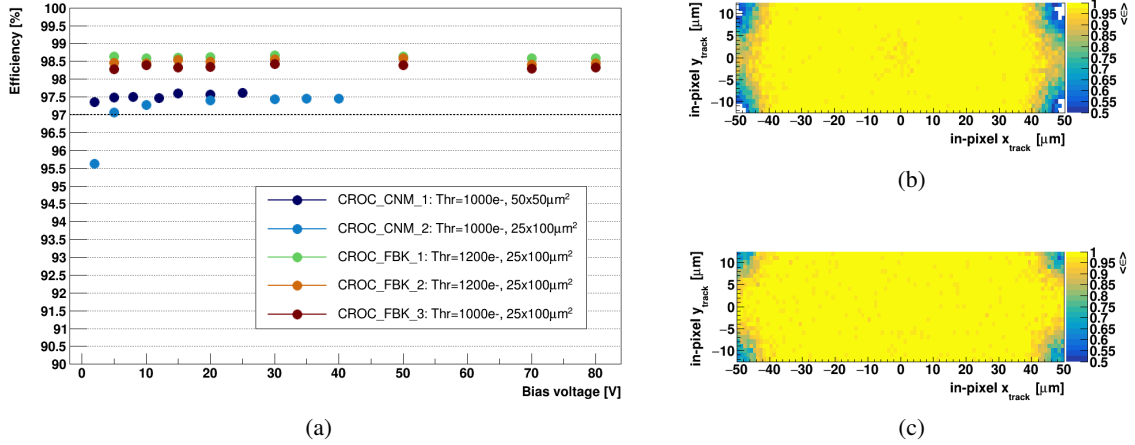


Figure 4: (a) Hit detection efficiency as a function of bias voltage for several non-irradiated modules. 97% efficiency is indicated by a dashed line. Pixel cell maps of efficiency for module CROC_CNМ_2 at a bias voltage of (b) 2 V and (c) 30 V.

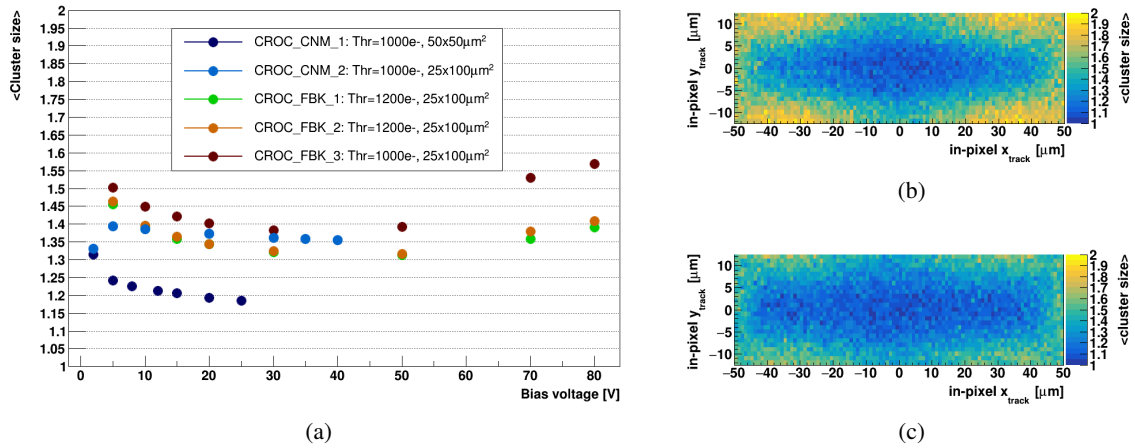


Figure 5: (a) Average cluster size as a function of bias voltage for several non-irradiated modules. Pixel cell maps of cluster size for module CROC_FBK_1 at a bias voltage of (b) 5 V and (c) 30 V.

The DUT spatial resolution is estimated from the residuals, defined as the differences between the track impact position on the DUT and the position of the assigned cluster. Consequently, the residual distribution is a convolution of the DUT spatial resolution and the telescope resolution. Figures 6a and 6b present examples of the residual distributions for the short (25 μm) and long (100 μm) pixel pitches, respectively. The width of the distribution for the short pixel pitch, typically obtained from a Gaussian fit, corresponds to the sum in quadrature of these two resolutions. However, this distribution exhibits tails, primarily due to misassociations between clusters and tracks. This artifact can be addressed using one of the following fitting models: the sum of two Gaussians, $N_1(\mu, \sigma_1^2) + N_2(\mu, \sigma_2^2)$, or the sum of a Gaussian and a constant term c , $N_1(\mu, \sigma_1^2) + c$. The mean of the standard deviations from the Gaussian fits to the core of the distribution, derived from both models, is taken as the effective width of the residual distribution in this analysis.

A data-driven approach is used to estimate the telescope resolution. Unlike on the residuals for the $25\ \mu\text{m}$ -pitch, the effects of charge sharing and telescope resolution on the residuals for the $100\ \mu\text{m}$ -pitch are disentangled, owing to low charge sharing across the short pixel pitch. Consequently, the telescope resolution is determined by fitting the edge of the residual distribution for the long pixel pitch to the cumulative distribution function of a Gaussian, $\Phi(\frac{x-\mu}{\sigma}) = \frac{1}{2}(1 + \text{erf}(\frac{x-\mu}{\sigma\sqrt{2}}))$. The standard deviation obtained from this fit, divided by the cosine of the angle, represents the telescope resolution at the DUT position. Figure 6c shows the spatial resolution on the short pixel pitch of the FBK modules as a function of the angle, defined as the rotation around an axis parallel to the long pixel pitch and perpendicular to the beam direction. The best resolution is about $2.5\ \mu\text{m}$.

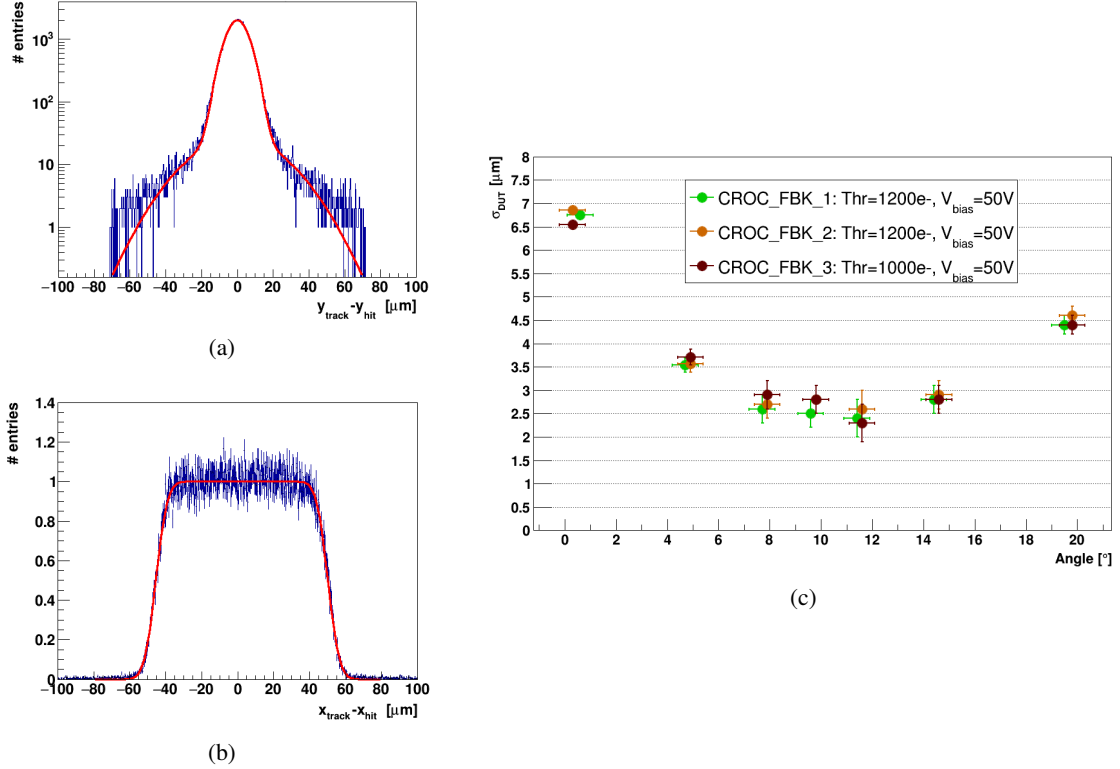


Figure 6: Example of the residual distribution for (a) the $25\ \mu\text{m}$ -pitch fitted to the sum of two Gaussians, and (b) the $100\ \mu\text{m}$ -pitch fitted to the difference between two cumulative distribution functions. (c) Spatial resolution on the short pixel pitch as a function of the rotation angle for several non-irradiated FBK modules biased at 50 V.

4 Methodology and test beam results of irradiated modules

The performance after irradiation of several modules with $25 \times 100\ \mu\text{m}^2$ pixel size was also evaluated in test beams. The thresholds of the modules irradiated up to fluences of $1 \times 10^{16}\ \text{n}_{\text{eq}}\text{cm}^{-2}$ and $1.6 \times 10^{16}\ \text{n}_{\text{eq}}\text{cm}^{-2}$ were tuned at a temperature of $-30\ ^\circ\text{C}$ to average pixel thresholds of $1000\ \text{e}^-$ and $1200\ \text{e}^-$, respectively. Pixels were masked using the same criteria described for non-irradiated devices. The FBK samples irradiated to the lowest fluence kept the percentage of masked pixels below 2% up to a bias voltage of 150 V, whereas the CNM sample exhibited a sharp increase at 130 V. At this voltage, the proportion of masked pixels in the CNM module decreased from 9% to

3 % when the threshold was raised to $1200 e^-$. In the more heavily irradiated device, the percentage of masked pixels remained below 3 % up to 130 V, but then rose steeply to 10 % at 140 V.

Figures 7a and 7b show the hit detection efficiency at normal beam incidence as a function of the bias voltage for modules irradiated to $1 \times 10^{16} n_{eq}cm^{-2}$ and $1.6 \times 10^{16} n_{eq}cm^{-2}$, respectively. 97 % efficiency is achieved by all modules, resulting in a wide operation range with a low number of masked pixels and excellent performance: around 50 V for modules irradiated to $1 \times 10^{16} n_{eq}cm^{-2}$ and 30 V for those irradiated to $1.6 \times 10^{16} n_{eq}cm^{-2}$. The efficiency corrected by the acceptance, which is defined as $1 - \frac{\text{No. of masked pixels}}{\text{No. of pixels}}$, is also illustrated in Fig. 7 to quantify the impact of masked pixels on the detection efficiency. Whenever the percentage of masked pixels sharply increases, the corrected efficiency significantly drops, as seen in Fig. 7b at the highest bias voltage.

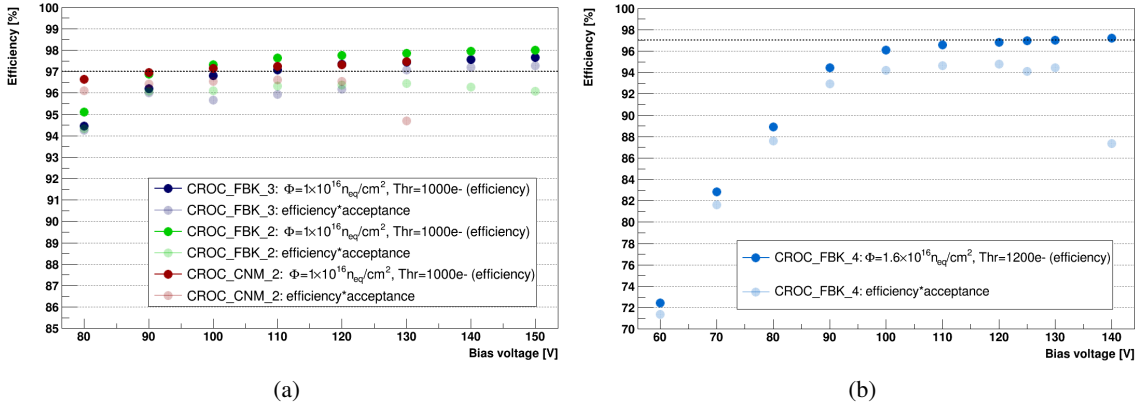


Figure 7: Hit detection efficiency with and without the acceptance correction as a function of the bias voltage for modules irradiated to (a) $1 \times 10^{16} n_{eq}cm^{-2}$ and (b) $1.6 \times 10^{16} n_{eq}cm^{-2}$. The solid colors show the efficiency, while the lighter colors represent the efficiency times the acceptance.

The dependence of the efficiency on the average pixel threshold to which the modules are tuned is shown in Fig. 8 for both fluences. This study was conducted at full depletion, normal beam incidence and without a pixel mask. The maximum efficiency drop observed in the less irradiated modules is 2 % when doubling the threshold, while it becomes 16 % for the heavily irradiated one. These results underline the importance of keeping the threshold as low as possible at high fluences.

Irradiation leads to a degradation in both the amount of collected charge and the spatial resolution of the devices. Figure 9a shows the cluster charge distribution at normal beam incidence for module CROC_FBK_2, irradiated to $1 \times 10^{16} n_{eq}cm^{-2}$ and biased at 130 V. The cluster charge MPV is around $5000 e^-$, indicating a 50 % reduction compared to the charge expected before irradiation. For the short pixel pitch, the best spatial resolution after irradiation to $1 \times 10^{16} n_{eq}cm^{-2}$ is approximately $3.5 \mu m$, as shown in Fig. 9b.

5 Conclusions

3D pixel sensors equipped with the prototype of the final readout chip have proven to have excellent performance, meeting all CMS requirements. After irradiation up to $1.6 \times 10^{16} n_{eq}cm^{-2}$, these devices maintain a hit detection efficiency above 97 % across a wide operation range, with a low average pixel threshold and a small number of masked pixels.

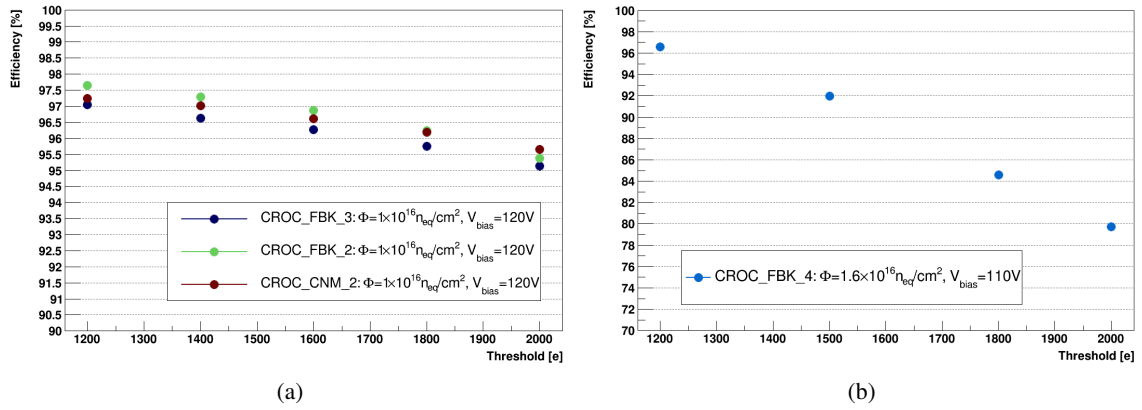


Figure 8: Hit detection efficiency as a function of the average pixel threshold for (a) modules irradiated to $1 \times 10^{16} \text{ n}_{\text{eq}}\text{cm}^{-2}$ at 120 V and (b) modules irradiated to $1.6 \times 10^{16} \text{ n}_{\text{eq}}\text{cm}^{-2}$ at 110 V.

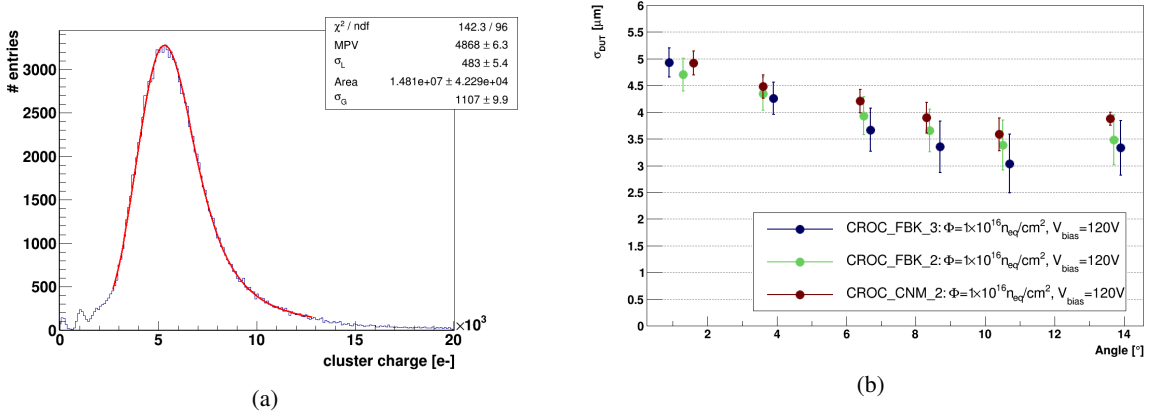


Figure 9: (a) Cluster charge distribution for module CROC_FBK_2 irradiated to $1 \times 10^{16} \text{ n}_{\text{eq}}\text{cm}^{-2}$ and biased at 130 V. It is fitted to a Landau distribution with most probable value MPV and width σ_L , convoluted with a Gaussian of width σ_G . (b) Spatial resolution on the short pixel pitch as a function of the rotation angle for modules irradiated to $1 \times 10^{16} \text{ n}_{\text{eq}}\cdot\text{cm}^{-2}$ and biased at 120 V.

References

- [1] CMS collaboration, *The Phase-2 Upgrade of the CMS Tracker*, Tech. Rep. [CERN-LHCC-2017-009](#), [CMS-TDR-014](#), CERN, Geneva (2017).
- [2] S. Parker et al., *3D — A proposed new architecture for solid-state radiation detectors*, *Nucl. Inst. Meth. A* **395** (1997) 328.
- [3] G.-F. Dalla Betta et al., *Small pitch 3D devices*, *PoS Vertex 2016* (2017) 028.
- [4] D. Quirion et al., *Manufacturability and Stress Issues in 3D Silicon Detector Technology at IMB-CNM*, *Micromachines* **11** (2020) .
- [5] RD53 collaboration, *RD53B Manual*, Tech. Rep. [CERN-RD53-PUB-19-002](#), CERN, Geneva (2019).
- [6] H. Jansen et al., *Performance of the EUDET-type beam telescopes*, *EPJ TECH INSTRUM* **3** (2016) .